

SOFT X-RAY SPECTROSCOPY OF NGC 1068 WITH *XMM-NEWTON* RGS AND *CHANDRA* LETGS

A. Kinkhabwala¹, M. Sako^{1,2,3}, E. Behar¹, S.M. Kahn¹, F. Paerels¹, A.C. Brinkman⁴, J.S. Kaastra⁴,
R.L.J. van der Meer⁴, M.F. Gu^{3,5}, D.A. Liedahl⁶

¹Columbia Astrophysics Laboratory, Columbia University, 550 West 120th Street, New York, NY 10027

²Theoretical Astrophysics and Space Radiation Laboratory, California Institute of Technology, MC 130-33, Pasadena, CA 91125

³Chandra Fellow

⁴Space Research Organization of the Netherlands, Sorbonnelaan 2, 3548 CA, Utrecht, The Netherlands

⁵Center for Space Research, Massachusetts Institute of Technology, Cambridge, MA, 02139

⁶Physics Department, Lawrence Livermore National Laboratory, P.O. Box 808, L-41, Livermore, CA 94550

ABSTRACT

1. INTRODUCTION

We present high-resolution soft-X-ray spectra of the prototypical Seyfert 2 galaxy, NGC 1068, taken with the *XMM-Newton* Reflection Grating Spectrometer (RGS) and the *Chandra* Low Energy Transmission Grating Spectrometer (LETGS). Its rich emission-line spectrum is dominated by recombination in a warm plasma (bright, narrow radiative recombination continua provide the “smoking gun”), which is photoionized by the inferred nuclear power-law continuum. Radiative decay following photoexcitation of resonant transitions also provides an important contribution. A self-consistent model of a photoionized and photoexcited cone of gas is capable of reproducing the hydrogenic/heliumlike ionic line series in detail. The ratio of photoexcitation to photoionization in the cone provides important geometric information such as the radial ionic column densities, which are consistent with absorption measurements (the warm absorber) in Seyfert 1 galaxies. This strongly suggests that the emission spectrum we observe from NGC 1068 emanates from its warm absorber. The observed extent of the ionization-cone/warm-absorber in NGC 1068 of about 300 pc implies that a large fraction of the gas associated with generic warm absorbers may typically exist on the hundreds-of-parsec scale rather than much closer to the nucleus (e. g., less than a parsec). Spatially-resolved spectroscopy using the LETGS of two distinct emission regions yields two noticeably different spectra. We show that these differences are solely due to differing radial column densities. A fairly flat distribution in ionization parameter $\xi = L_X/n_e r^2$ (over at least $\log \xi \sim 0-3$) is necessary to explain the inferred radial ionic column densities of all spectra. We show that this must primarily be due to a broad density distribution $f(n_e) \propto n_e^{-1}$ at each radius, spanning roughly $n_e \sim 0.1-100 \text{ cm}^{-3}$. Additional contributions to the soft-X-ray emission from hot, collisionally-ionized gas, if present, make a negligible contribution to the spectrum.

Key words: galaxies: individual (NGC 1068) — galaxies: Seyfert — line: formation — X-rays: galaxies

In the unified model of active galactic nuclei (AGN), the observational properties of a particular AGN are determined simply by its orientation (Miller & Antonucci 1983; Antonucci & Miller 1985). For Seyfert 1 galaxies, we directly observe the intrinsic nuclear continuum, partially absorbed by photoionized outflowing material (warm absorber). We observe Seyfert 2 galaxies at an angle nearly perpendicular to the Seyfert 1 orientation. From this vantage, the intrinsic nuclear continuum is highly obscured (by the “dusty torus”), and the spectrum is dominated by reprocessed emission from outlying clouds filling an ionization cone, which may be related to the warm absorber.

The first high-resolution soft-X-ray spectrum obtained of a Seyfert 2 galaxy was the *Chandra* HETGS of Markarian 3 (Sako et al. 2000). Sako et al. (2000) interpreted the bulk of this spectrum as due to recombination/radiative cascade following photoionization. Radiative decay following photoexcitation is also required to explain the enhanced resonance lines in the heliumlike triplets. This is consistent with outlying clouds irradiated by the inferred nuclear continuum, as predicted in the unified model Krolik & Kriss (1995).

We present below the first high-resolution X-ray spectrum of the X-ray-brightest, prototypical Seyfert 2 galaxy, NGC 1068, which was obtained with *XMM-Newton* RGS (Kinkhabwala et al. 2002b). Using a simple model of an irradiated gas cone, we are able to find an excellent fit to the detailed soft X-ray spectrum of NGC 1068 (for all hydrogenic/heliumlike ions). From the similarity of our inferred radial column densities to directly-measured absorption column densities (warm absorber) in Seyfert 1 galaxies, we argue that the observed hundreds-of-parsec-scale ionization cone of NGC 1068 is identical to the warm absorber in this AGN. A subsequent spectrum obtained with the *Chandra* LETGS (Brinkman et al. 2002) confirms the RGS results, but, more importantly, allows for spatially-resolved spectroscopy of this extended source.

2. FULL RGS/LETGS SPECTRA OF NGC 1068

Line emission dominates the RGS/LETGS soft-X-ray spectra of NGC 1068 shown in Fig. 12 (for ease of comparison, all spectral plots appear at the end of the paper). Emission lines from hydrogenic and heliumlike C, N, O, Ne, Mg, Si, and S are all clearly detected. Fe L-shell emission lines from Fe XVII to Fe XXIV are present as well (unlabelled), with numerous transitions scattered between 9 Å and 18 Å. Many higher-order resonant transitions ($1s \rightarrow np$) in the hydrogenic and heliumlike ions labelled β - δ are prominent, with evidence for strong emission from even higher order transitions as well. Several unidentified features at longer wavelengths (e. g., at 27.92, 30.4, 34.0–34.6, and 36.38 Å) are likely due to L-shell emission from mid-Z ions such as sulfur. The fluorescent lines of neutral Fe (Fe^+0) and Si (Si^+0) are clearly detected in the LETGS spectrum. We see no significant continuum emission in the spectrum.

All lines appear broader than expected for a monochromatic source and several lines show evidence for significant blue shifts. These are due to intrinsic velocity distributions (hundreds of km/s) and are not instrumental effects.

The spectrum also includes very prominent radiative recombination continua (RRC) for hydrogenic and heliumlike C, N, and O, which are produced when electrons recombine directly to the ground state in these highly-ionized ions. RRC are smeared out for hot collisionally-ionized gas, but are narrow, prominent features for cooler photoionized gas. The narrow width of these RRC provide a direct measure of the recombining electron temperature (Liedahl & Paerels 1996; Liedahl 1999), which for NGC 1068 is $kT \sim 2 - 10$ eV.

3. MODEL OF IRRADIATED GAS CONE

We have constructed a fully self-consistent model of a gas cone (warm absorber) irradiated by a continuum source (Fig. 1). The nuclear region comprising the black-hole/accretion-disc/comptonized-halo system is depicted as the central black circle. Obscuration by the “dusty torus” is shown (in cross section) as two clouds on either side of the nucleus. The parameters which comprise our two inferred global model parameters, the covering factor times nuclear luminosity fL_X and the radial velocity width σ_v^{rad} , are indicated, as well as the individual radial ionic column densities $N_{\text{ion}}^{\text{rad}}$. L_X is the total luminosity in a power-law with reasonable values for the index of $\Gamma = -1.7$ and energy range of 13.6 eV–100 keV.

Photoionization and photoexcitation in the ionization cone produce absorption features (warm absorber) in the Seyfert 1 view, but in the Seyfert 2 view, the inverse processes of recombination/radiative cascade and radiative decay, respectively, produce line emission (Fig. 2). We use the new atomic code FAC (Gu 2002) to calculate the relevant atomic data for hydrogenic/heliumlike ions. For ease

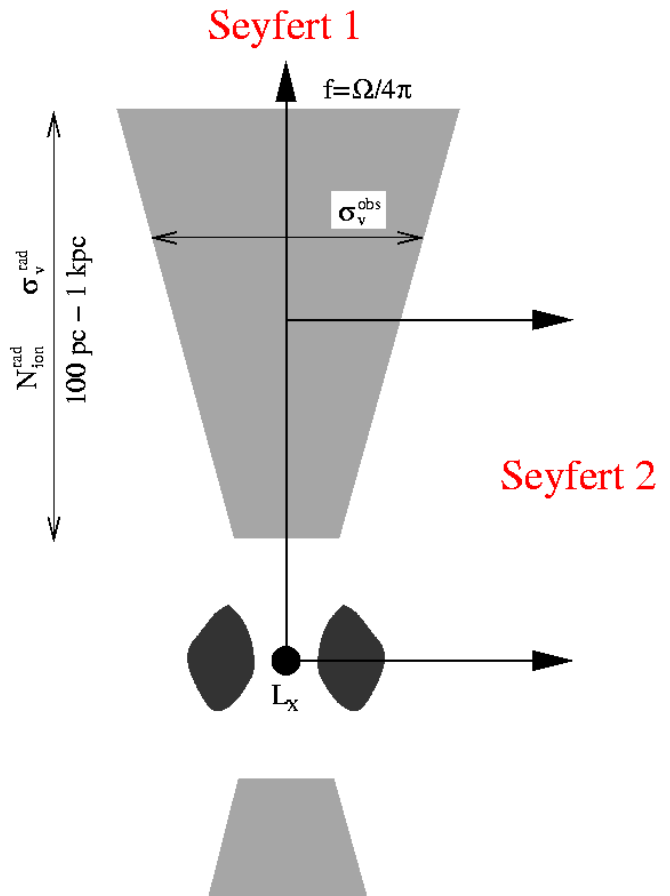


Figure 1. Schematic of our unified, warm-absorber/ionization-cone model for Seyfert 1 and 2 galaxies (not to scale). The labels “Seyfert 1” and “Seyfert 2” indicate the directions of the observer in the two cases.

of fitting, we have incorporated our model into XSPEC (Arnaud 1996) as a local model (“photo”). A complete discussion of the atomic calculations and astrophysical assumptions underlying our model is presented in Kinkhabwala et al. (2002a).

For the specific case of NGC 1068, the intrinsic continuum is likely to be completely obscured, contributing no flux to the soft X-ray regime. Also, the NE cone is much brighter than its counterpart in the SW (Young et al. 2001), therefore, the covering factor f applies to the NE cone alone (hence the asymmetry of Fig. 1).

3.1. COLUMN DENSITY

We show the effect of varying the radial ionic column density on O VII in Fig. 3. The top three panels on the left show the radial “Seyfert 1” view through the outflow and down to the nucleus for radial column densities in O VII of 10^{15} , 10^{17} , and 10^{19} cm^{-2} . The corresponding top three panels on the right show the “Seyfert 2” view roughly

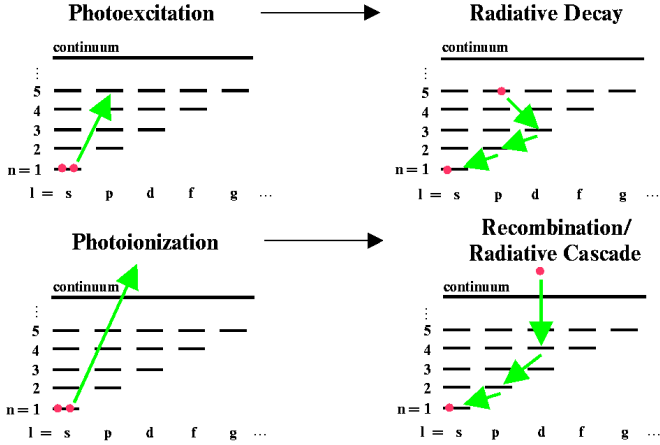


Figure 2. Simplified Grotrian diagram of the relevant atomic processes in hydrogenic/heliumlike ions. Photoexcitations and photoionizations appear as absorption features in the Seyfert 1 view (left), but as line emission through the inverse processes of radiative decay and recombination/radiative cascade in the Seyfert 2 view (right).

perpendicular to the axis of outflow and from which the nucleus is completely obscured (Fig. 1). All photons absorbed out of the power law in the ‘‘Seyfert 1’’ spectrum are reprocessed and reemitted to generate the ‘‘Seyfert 2’’ spectrum. Radiative decay following photoexcitation dominates the ‘‘Seyfert 2’’ spectrum at low column densities, whereas recombination/radiative cascade following photoionization dominates at high column densities (for comparison, pure recombination is shown in the lower right panel). For hydrogenic ions, the behavior is similar (omitting the intercombination/forbidden lines).

3.2. VELOCITY WIDTH

In Fig. 4, we show the effect of varying the radial velocity width for O VII. Larger σ_v^{rad} enhance the importance of photoexcitation relative to photoionization.

4. MODEL FIT TO THE RGS SPECTRUM

We present our fit to the RGS spectrum of NGC 1068 in Fig. 13. The parameters used for the fit are given in the first column of Table 1. To convert observed flux to luminosity for the spectra of NGC 1068, we assume a distance of 14.4 Mpc (Bland-Hawthorn et al. 1997). The column density of neutral hydrogen in our galaxy is taken to be $N_H = 1e20 \text{ cm}^{-2}$ (using the high-quality soft-X-ray spectrum itself), which is somewhat lower than the standard column density to this source (Kinkhabwala et al. 2002b). For all fits in this paper, we assume recombining electron temperatures of $kT = 2.5 \text{ eV}$ for C V, $kT = 3 \text{ eV}$ for N VI, $kT = 4 \text{ eV}$ for C VI, N VII, O VIII, and O VIII,

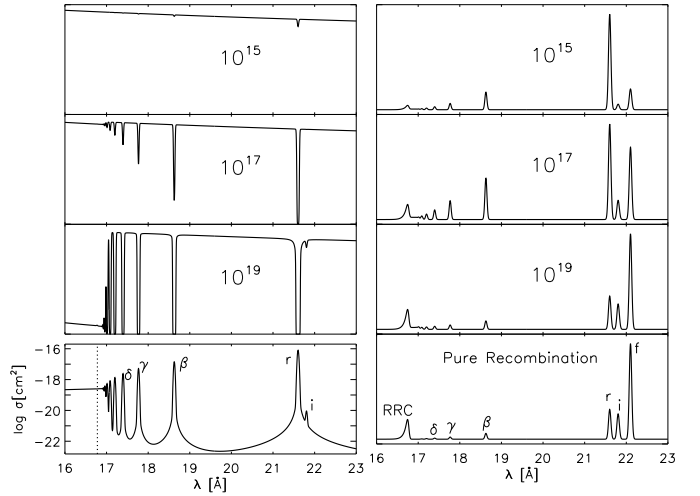


Figure 3. Effect of differing radial column densities on the reemitted spectrum for O VII with the Seyfert 1 view in the top three panels on the left and the Seyfert 2 view in the corresponding top three panels on the right. The bottom left panel shows ionic cross section with the photoexcitation/photoionization boundary indicated. The bottom right panel shows the spectrum expected for pure recombination. All spectral axes are linear, but have arbitrary normalization. Throughout, we take a radial gaussian distribution with $\sigma_v^{\text{rad}} = 200 \text{ km/s}$, transverse velocity distribution with $\sigma_v^{\text{obs}} = 400 \text{ km/s}$, and temperature $kT = 3 \text{ eV}$.

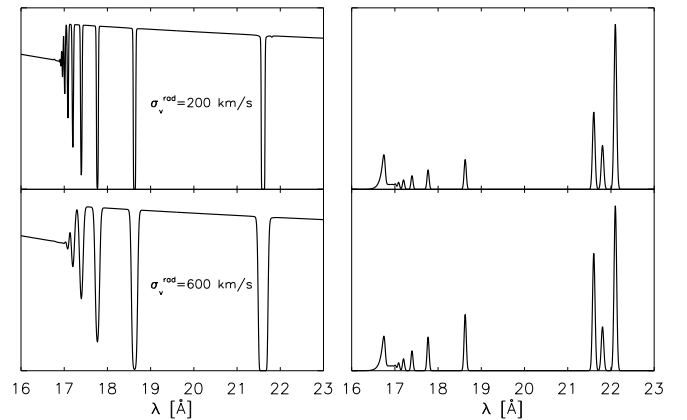


Figure 4. The effect of different σ_v^{rad} for the O VII spectrum using $N_{\text{ion}}^{\text{rad}} = 10^{18} \text{ cm}^{-2}$, with the Seyfert 1 view on the left and the Seyfert 2 view on the right. Spectra on the right-hand-side were convolved with the same transverse velocity distribution $\sigma_v^{\text{obs}} = 400 \text{ km/s}$; we also assume $kT = 3 \text{ eV}$.

and $kT = 10 \text{ eV}$ for all other ions (which have poorly-determined RRC).

Velocity broadening of all model emission lines by $\sigma_v^{\text{obs}} = 400 \text{ km/s}$ is necessary to fit the observed lines.

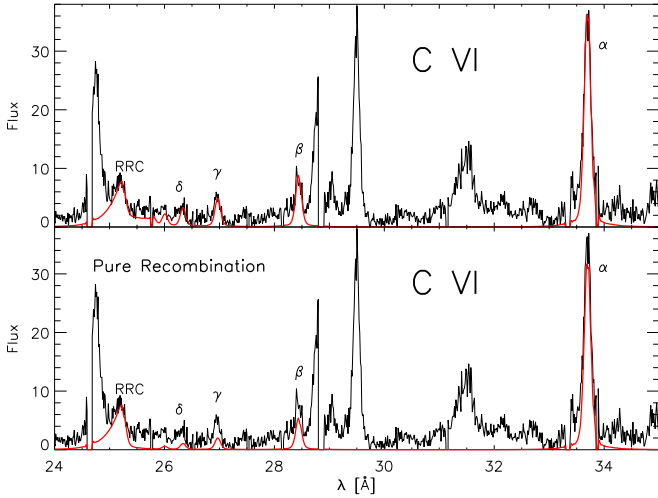


Figure 5. The final fit to C VI including recombination/radiative cascade following photoionization and radiative decay following photoexcitation (top). Recombination alone (bottom) is unable to explain the excess emission in all resonant lines $np \rightarrow 1s$.

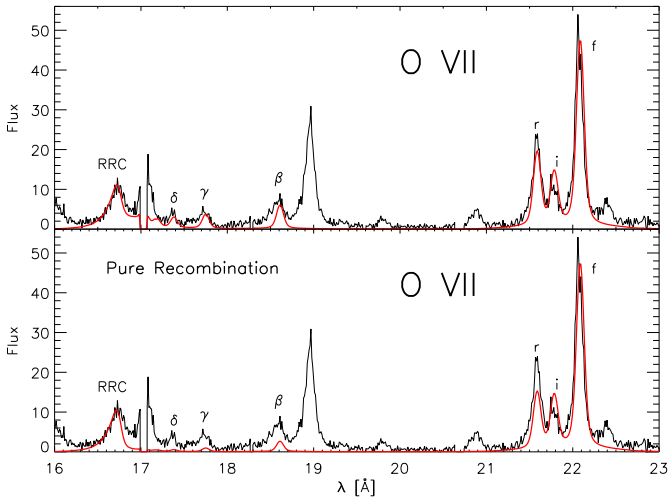


Figure 6. The final fit to O VII including recombination/radiative cascade following photoionization and radiative decay following photoexcitation (top). Recombination alone (bottom) is unable to explain the excess emission in all resonant lines $np \rightarrow 1s$.

We illustrate the relative contributions of photoionization and photoexcitation to the ionic line series for C VI and O VII in Figs. 5 and 6, respectively. Pure recombination is unable to explain the anomalous strength of the higher-order-series transitions. However, the self-consistent addition of photoexcitation allows for an excellent overall fit. An additional collisional gas component *instead* of photoexcitation would be insufficient to explain the higher-order series transitions (Fig. 7).

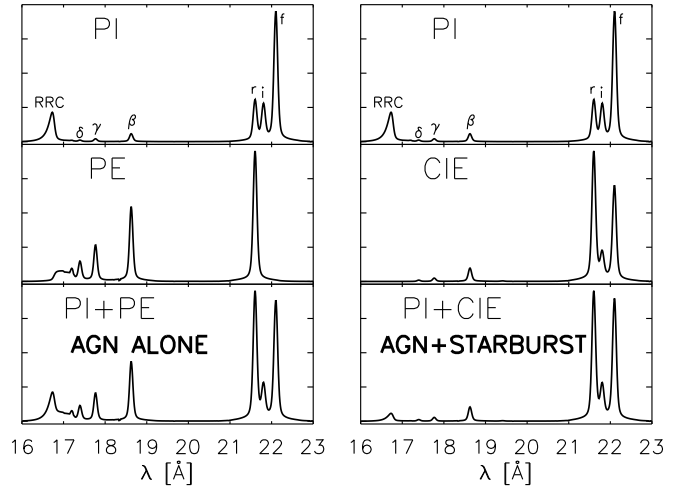


Figure 7. We demonstrate how to distinguish between hot collisional gas (e. g., starburst region) and photoexcitation. Starting with pure recombination following photoionization (“PI” - top two panels, $kT = 4$ eV), we self-consistently add radiative decay following photoexcitation (“PE”- middle left panel) assuming reasonable ionization cone parameters, or an additional hot gas component in collisional ionization equilibrium (“CIE” - middle right panel, $kT = 150$ eV) to obtain the bottom two panels. Note that both bottom panels have similar triplet ratios, implying that using the triplet alone is insufficient to discriminate between these two scenarios. However, the “AGN ALONE” panel has significantly stronger higher-order-series transitions (including the RRC) than the “AGN+STARBURST” panel, demonstrating the diagnostic importance of these transitions. (Normalization in each panel is arbitrary.)

5. LETGS SPATIALLY-RESOLVED SPECTROSCOPY

With the LETGS, it is possible to perform spatially-resolved spectroscopy by making cuts in the cross dispersion direction. NGC 1068 provides perhaps the best example of this capability, since it shows evidence for two fairly separated emission regions, which we denote simply as “primary” and “secondary.” The two cross-dispersion regions we use for the “primary” and “secondary” spots are shown in Figs. 8 and 9.

Spectra of the “primary” and “secondary” spots are given in Figs. 14 and 15, respectively, along with their corresponding best fit models. The fit parameters we obtain are given in Table 1. The same fL_X parameter works fairly well for all spectra, however a slightly different radial velocity width σ_v^{rad} is preferred by the “primary” spectrum. This illustrates the relative factor-of-two uncertainty in all fit parameters. However, this uncertainty does not affect any of our conclusions. All LETGS models have been convolved with the specific zero-order dispersion profile.

Table 1. Fit parameters for Figs. 13, 14, and 15. ‘H’ and ‘He’ indicate hydrogenic and heliumlike, respectively.

		RGS	Primary	Secondary
fL_X [ergs/s]		1e43	1e43	1e43
σ_v^{rad} [km/s]		100	60	100
Ion	H/He	Column Densities $N_{\text{ion}}^{\text{rad}}$ [cm^{-2}]		
C V	He	5e17	4.5e17	2e17
C VI	H	7e17	6e17	1.5e17
N VI	He	4e17	2.5e17	8e16
N VII	H	6e17	4e17	8e16
O VII	He	9e17	7e17	1.5e17
O VIII	H	1e18	6e17	2.5e17
Ne IX	He	3e17	2.5e17	6e16
Ne X	H	2.5e17	1.5e17	6e16
Mg XI	He	2e17	1.2e17	1e16
Mg XII	H	2e17	8e16	1e16
Si XIII	He	2e17	2e17	2e16
Si XIV	H	2e17	1.8e17	2e16
S XV	He	—	6e16	1e16
S XVI	H	—	9e16	1e16

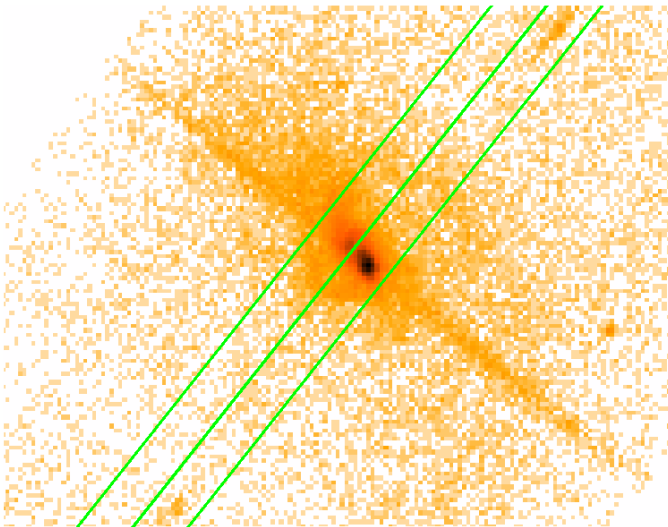


Figure 8. Zero-order LETGS image (logarithmic) of NGC 1068 oriented with N up and E to the left. There are two general regions which we denote as the “primary” (brightest spot) and “secondary” (accompanying NE spot). The dispersion axis is parallel to the green lines, which demarcate the cross dispersion regions we used to generate the “primary” and “secondary” spectra. The apparent line of emission in the cross-dispersion direction and centered on the source is instrumental (due to CCD readout). The high-energy edge of the dispersed spectrum can be seen in the upper right and lower left of the image.

The “secondary” spot, which is roughly coincident with the radio outflow lobes and the edge of the UV ionization cone, exhibits a noticeably different spectrum from the “primary” spot. The heliumlike resonance lines of Ne

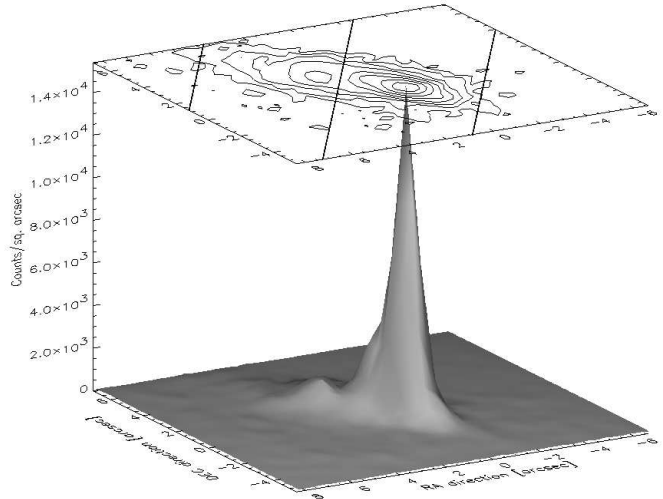


Figure 9. Zero-order LETGS image of NGC 1068. The relative brightness of the “primary” and “secondary” spots are clearly shown. The straight lines in the “factors-of-two” contour image are the same as the green lines in Fig. 8, denoting the extraction regions for the “primary” and “secondary” spectra.

and O are relatively stronger compared to the forbidden lines than in the “primary” spot. This enhancement might be due to an additional collisional component, perhaps outflow-shock-heated gas. However, this is ruled out by the strength of several higher-order-series lines and the normalization of the heliumlike intercombination/forbidden lines to the RRC (see Fig. 7 for an explanation). The observed enhancements are in fact simply due to a *lower* column density through the material (Fig. 3).

6. CONCLUSIONS

We have shown that the *XMM-Newton* RGS spectrum of the soft-X-ray emission from NGC 1068 is due entirely to recombinations and radiative cascade in an ionized gas cone, which is photoionized and photoexcited by the inferred nuclear continuum. A simple model of a warm, photoionized cone is capable of explaining all hydrogenic and heliumlike ion spectra *in detail*. The values we infer for the radial ionic column densities are similar to column densities observed in absorption (warm absorber) in Seyfert 1 galaxies (Kaastra et al. 2000; Kaspi et al. 2000; Branduardi-Raymont 2001; Sako et al. 2001). Since the ionization cone in NGC 1068 is spread over a region of ~ 300 pc (Young et al. 2001), this implies that generic warm absorbers have typical sizes of hundreds of parsec, rather than existing very close (e. g., < 1 pc) to the nucleus. A subsequent spectrum obtained with *Chandra* LETGS confirms the RGS results for the spectrum of the entire object, but also allows for spatially-resolved spectroscopy of the two bright spots resolved in the zero-order

image. The difference in spectra between these two spots is due entirely to different radial ionic column densities, and not, for example, to an additional contribution from hot, outflow-shocked gas. In Fig. 10, we show that the temperatures we obtain for all spectra using well-measured, non-blended RRC are fairly consistent with (though slightly higher than) temperatures predicted from a self-consistent simulation using XSTAR (Kallman & Krolik (1995)) of an optically-thin photoionized plasma.

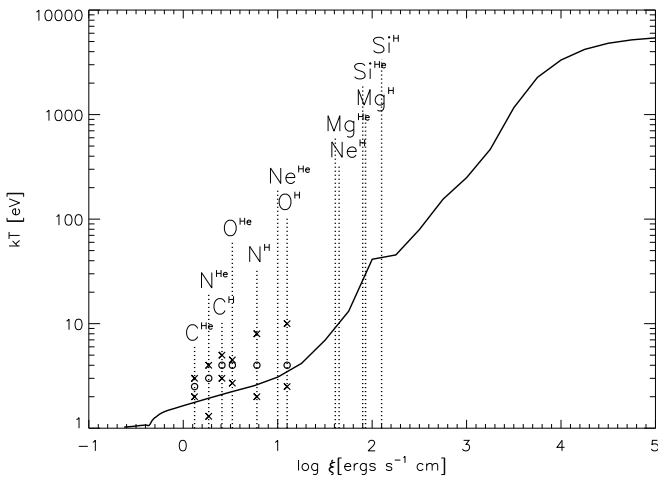


Figure 10. Recombination emissivity peak (for formation of the H^- - or He^- -like ionic species) calculated using XSTAR with incident power-law spectrum ($\Gamma = -1.7$, $13.6 \text{ eV} < E < 100 \text{ keV}$). The FWHM of the emissivity for each ion is $\Delta \xi \sim 1$. The x 's and o 's give the confidence interval and best fit, respectively, for each ion temperature measured from the ion RRC.

The ionic column densities we infer allow us to probe the ionization parameter distribution of the gas. We show the predicted fractional ionic abundances as a function of ionization parameter $\xi = L_X/n_e r^2$ in Fig. 11. We point out the relatively equal column densities inferred for the hydrogenic and heliumlike species of each element in each spectrum in Table 1. No single ionization parameter is capable of reproducing this result. Instead, a rather flat distribution in ionization parameter is necessary. This could be obtained by assuming a spatially-stratified, single-density ionization cone (hence varying only r) or assuming an intrinsic density distribution at each radius. The striking overlap of O III and soft-X-ray emission regions in NGC 1068 (Young et al. 2001) coupled with the presence of a similar range of ions in the “primary” and “secondary” spots, which are located at different distances from the nucleus, favor the latter interpretation. The distribution in ξ then is mostly due to a distribution in n_e of $f(n_e) \propto n_e^{-1}$ over several orders of magnitude (roughly $n_e \sim 0.1\text{--}100$) at each radius (Kinkhabwala et al. 2002b; Brinkman et al. 2002).

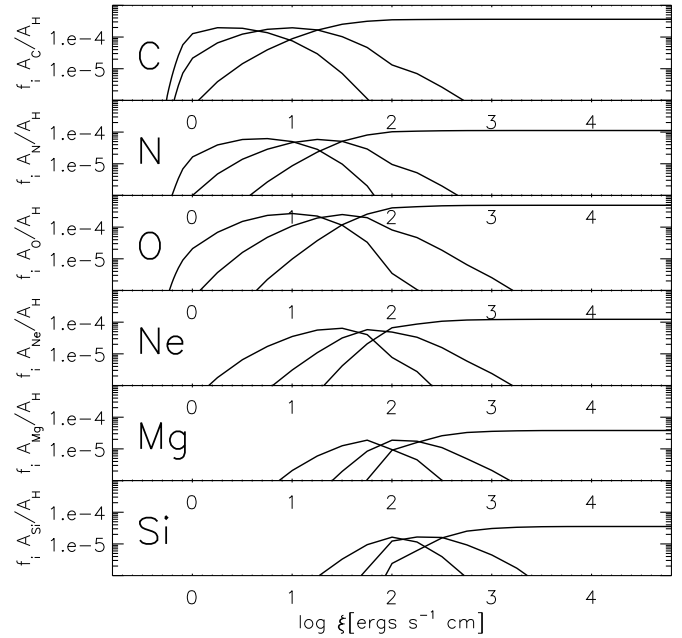


Figure 11. Fractional ionic abundances for the heliumlike (left), hydrogenic (middle), and bare (right) charge states for several ions as a function of ionization parameter $\xi = L_X/n_e r^2$.

ACKNOWLEDGEMENTS

This work is based on observations obtained with *XMM-Newton*, an ESA science mission with instruments and contributions directly funded by ESA Member States and the USA (NASA). The Columbia University team is supported by NASA. AK acknowledges additional support from an NSF Graduate Research Fellowship and NASA GSRP fellowship. MS and MFG were partially supported by NASA through *Chandra* Postdoctoral Fellowship Award Numbers PF01-20016 and PF01-10014, respectively, issued by the *Chandra* X-ray Observatory Center, which is operated by the Smithsonian Astrophysical Observatory for and behalf of NASA under contract NAS8-39073. SRON is supported by the Netherlands Foundation for Scientific Research (NWO). Work at LLNL was performed under the auspices of the U. S. Department of Energy, Contract No. W-7405-Eng-48.

REFERENCES

- Antonucci, R. R. J., & Miller, J. S. 1985, *ApJ*, 297, 621
- Arnaud, K. A. 1996, in *ASP Conf. Ser. 101, Astronomical Data Analysis Software Systems V*, ed. G. H. Jacoby & J. Barnes (San Francisco: ASP), 17
- Bland-Hawthorn, J., Gallimore, J. F., Tacconi, L. J. et al. 1997, *Ap&SS*, 248, Issue 1/2, 9
- Branduardi-Raymont, G., Sako, M., Kahn, S. M. et al. 2001, *A&A*, 365, L140
- Brinkman, A. C., Kaastra, J. S., van der Meer, R. et al. 2002 (in preparation)
- Gu, M.-F. 2002 (in preparation)

- Kaastra, J. S., Mewe, R., Liedahl, D. A., Komossa, S., & Brinkman, A. C. 2000, *A&A*, 354, L83
- Kallman, T. R., & Krolik, J. H. 1995, XSTAR = A Spectral Analysis Tool, HEASARC (NASA/GSFC, Greenbelt)
- Kaspi, S., Brandt, W. N., Netzer, H. et al. 2000, *ApJ*, 535, L17
- Kinkhabwala, A., Behar, E., Sako, M. et al. 2002a (in preparation)
- Kinkhabwala, A., Sako, M., Behar, E. et al. 2002b (in preparation)
- Krolik, J. H., & Kriss, G. A. 1995, *ApJ*, 447, 512
- Liedahl, D. A. 1999, in *X-Ray Spectroscopy in Astrophysics*, ed. J. van Paradijs & J. A. M. Bleeker (Berlin: Springer), 189
- Liedahl, D. A., & Paerels, F. 1996, *ApJ*, 468, L33
- Miller, J. S., & Antonucci, R. R. J. 1983, *ApJ*, 271, L7
- Sako, M., Kahn, S. M., Behar, E. et al. 2001, *A&A*, 365, L168
- Sako, M., Kahn, S. M., Paerels, F., & Liedahl, D. A. 2000, *ApJ*, 543, L115
- Young, A. J., Wilson, A. S., & Shopbell, P. L. 2001, *ApJ*, 556,

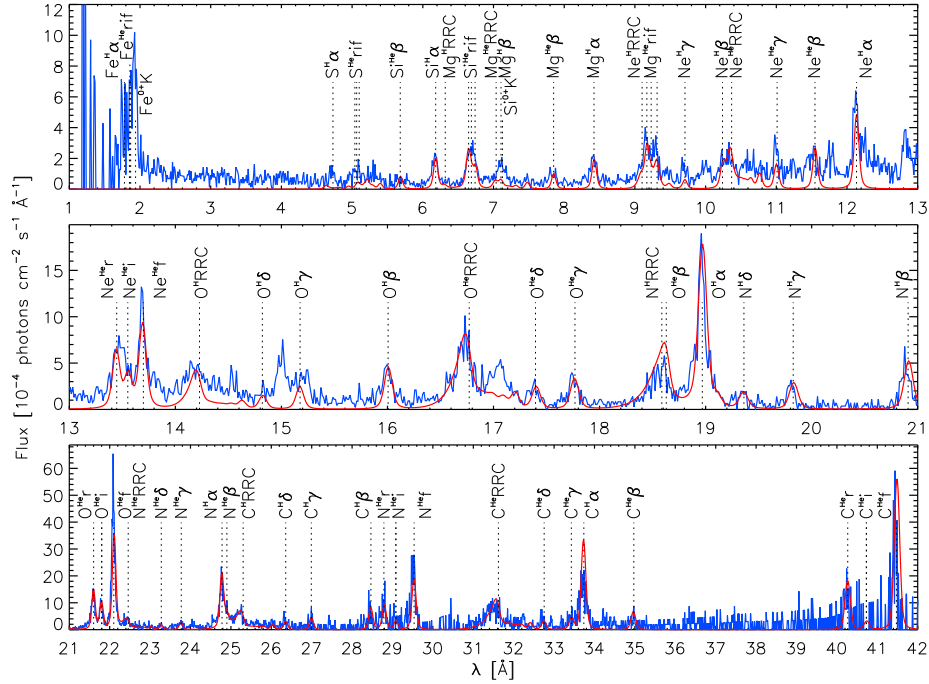


Figure 14. LETGS spectrum ($m=-1/+1$ orders) of the “primary” spot (blue) and corresponding hydrogenic/heliumlike ion fit (red) using parameters listed in Table 1. The spectrum has been shifted to the NGC 1068 rest frame ($z = 0.00379$). Model wavelengths are those expected for no excess velocity shifts. We employ the same labelling convention as in Fig. 12.

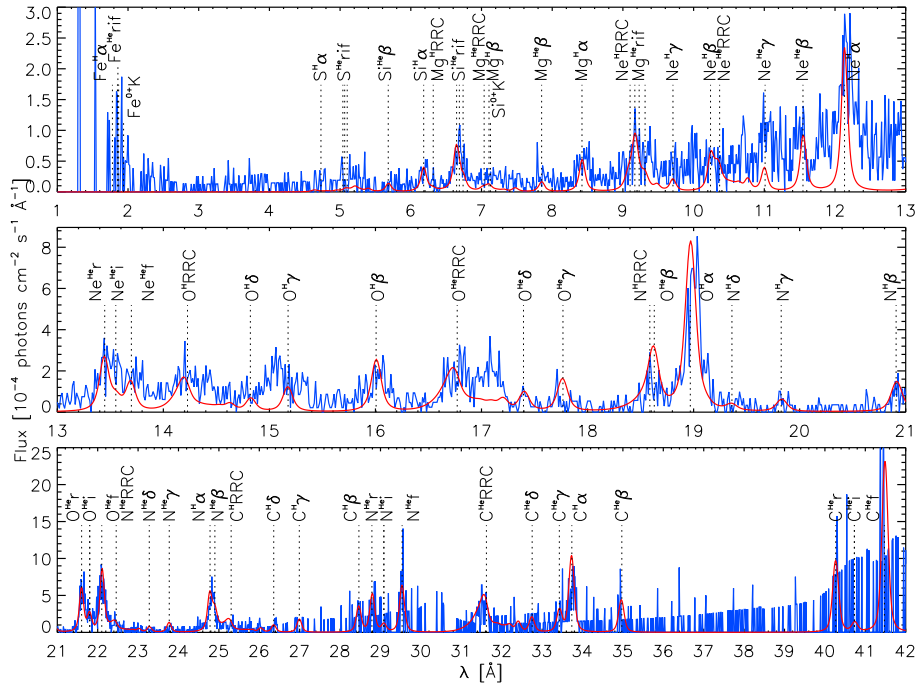


Figure 15. LETGS spectrum ($m=-1/+1$ orders) of the “secondary” spot (blue) and corresponding hydrogenic/heliumlike ion fit (red) using parameters listed in Table 1. The spectrum has been shifted to the NGC 1068 rest frame ($z = 0.00379$). Model wavelengths are those expected for no excess velocity shifts. We employ the same labelling convention as in Fig. 12. Note the enhanced resonance line in the O and Ne heliumlike triplets. Several higher-order ($np \rightarrow 1s$, $n > 2$) lines also appear (e. g., $^1\text{O}^{\text{He}}\delta$ and $^1\text{N}^{\text{H}}\gamma$), providing clear evidence for photoexcitation rather than an additional hot, collisional gas component (see Fig. 7).